Author Manuscript

Author Manuscript

Author Manuscript

Author Manuscript

HHS Public Access

Author manuscript

Magn Reson Med. Author manuscript; available in PMC 2020 June 18.

Published in final edited form as:

Magn Reson Med. 2019 October ; 82(4): 1385–1397. doi:10.1002/mrm.27819.

Optimized quantification of spin relaxation times in the hybrid state

Jakob Assländer[1,2], **Riccardo Lattanzi**[1,2,3], **Daniel K. Sodickson**[1,2,3], **Martijn A. Cloos**[1,2,3]

[1]Center for Biomedical Imaging, Department of Radiology, New York University School of Medicine, New York, New York

[2]Center for Advanced Imaging Innovation and Research (CAI2R), Department of Radiology, New York University School of Medicine, New York, New York

[3]Sackler Institute of Graduate Biomedical Sciences, New York University School of Medicine, New York, New York

Abstract

Purpose—The optimization and analysis of spin ensemble trajectories in the hybrid state—a state in which the direction of the magnetization adiabatically follows the steady state while the magnitude remains in a transient state.

Methods—Numerical optimizations were performed to find spin ensemble trajectories that minimize the Cramér-Rao bound for T_1-encoding, T_2-encoding, and their weighted sum, respectively, followed by a comparison between the Cramér-Rao bounds obtained with our optimized spin-trajectories, Look-Locker sequences, and multi-spin-echo methods. Finally, we experimentally tested our optimized spin trajectories with in vivo scans of the human brain.

Results—After a nonrecurring inversion segment on the southern half of the Bloch sphere, all optimized spin trajectories pursue repetitive loops on the northern hemisphere in which the beginning of the first and the end of the last loop deviate from the others. The numerical results obtained in this work align well with intuitive insights gleaned directly from the governing equation. Our results suggest that hybrid-state sequences outperform traditional methods. Moreover, hybrid-state sequences that balance T_1- and T_2-encoding still result in near optimal signal-to-noise efficiency for each relaxation time. Thus, the second parameter can be encoded at virtually no extra cost.

Conclusions—We provided new insights into the optimal encoding processes of spin relaxation times in order to guide the design of robust and efficient pulse sequences. We found that joint acquisitions of T_1 and T_2 in the hybrid state are substantially more efficient than sequential encoding techniques.

Correspondence: Jakob Assländer, Center for Biomedical Imaging, Department of Radiology, New York University School of Medicine, 650 1st Avenue, New York, NY 10016. jakob.asslaender@nyumc.org.

SUPPORTING INFORMATION

Additional supporting information may be found online in the Supporting Information section at the end of the article.

Author Manuscript Author Manuscript Author Manuscript Author Manuscript

Keywords

HSFP; MRF; optimal control; parameter mapping; quantitative MRI; SSFP

1 | INTRODUCTION

The dynamics of large spin-1/2 ensembles in a magnetic field are commonly described by the Bloch equations, which capture the macroscopic effects of spin-lattice and spin-spin interactions with the characteristic time constants T_1 and T_2, respectively. Robust and rapid quantification of these parameters may lead to more objective diagnoses, improved longitudinal studies, and simplify computer aided diagnosis. The large dynamic range of inversion-recovery experiments makes them a natural choice for quantitative T_1 mapping. Similarly, a series of spin-echo experiments with varying echo times probe a wide dynamic range for estimating T_2. Both methods effectively strive to trace exponential relaxation curves following a single perturbation from thermal equilibrium—without being affected by the other relaxation time. However, T_1 and T_2 can also—and arguably more efficiently—be estimated by measuring magnetization in various steady-state conditions,[2–5] or even in more complex conditions that depart from the steady state.[6–8] Magnetic Resonance Fingerprinting (MRF),[8] e.g., opened a door for flexible parameter mapping and initiated various research efforts to increase the signal-to-noise ratio (SNR) efficiency of quantitative MRI. However, the large number of design options for MRF pulse sequences has limited the optimization of MRF experiments to heuristic approaches.[1,8–12] Furthermore, the lack of an intuitive understanding of the spin dynamics in MRF, and the over-simplified nature of the Bloch models employed in typical MRF implementations, creates a risk of introducing biases in the estimated relaxation times.[11] We have recently analyzed the biases introduced by inhomogeneities of the RF-excitation field $\left(B_1^+\right)$ and the main magnetic field (B_0), including intra-voxel dephasing, which is also known as inhomogeneous broadening.[13] It is known that this sensitivity to inhomogeneities originates from the magnetization component orthogonal to the steady-state magnetization.[14] Therefore, we derived an upper bound for variations of the flip angle and the phase increment of the RF-pulses that forces the direction of the magnetization to adiabatically follow the steady state. We found that this adiabaticity condition is considerably less stringent than the condition that ensures adiabaticity of the magnetization's magnitude (cf. Ref. 13 for details). Flip angle variations in between these bounds result in a so-called *hybrid state*, which combines the steady state's robustness—by virtue of the direction's adiabaticity—with the efficiency of the transient state—by virtue of the magnitude's diabaticity, i.e. non-adiabaticy.[13]

The adiabaticity of the magnetization's direction effectively decouples the Bloch equations when formulated in spherical coordinates. The angular dimension can be described by the well-established steady-state equations,[15,16] whereas the entire spin dynamics is trapped in the radial dimension, i.e., in the magnitude of the magnetization. Section 2.1 recaps and visualizes the hybrid-state equation of spin motion, which is the decoupled Bloch equation along the radial dimension, and highlights that the polar angle is the effective force that drives these dynamics. Thereafter, we provide an in-depth analysis of hybrid-state sequences and discuss how relaxation times can be encoded efficiently with this approach. By

Author Manuscript Author Manuscript Author Manuscript Author Manuscript

comparing hybrid-state sequences that were optimized to encode either T_1 or T_2 alone against those that resulted from joint optimizations, we show that the second parameter can be measured at virtually no extra cost.

2 | METHODS

2.1 | Hybrid-state spin dynamics

We start by describing the spin dynamics in spherical coordinates,[16] which are here defined by $x = r\sin\vartheta\cos\varphi$, $y = r\sin\vartheta\sin\varphi$ and $z = r\cos\vartheta$, where r is the radius, ϑ the polar angle or the angle between the magnetization and the z-axis and φ the azimuth or the angle between the x-axis and the projection of the magnetization onto the x-y-plane. For practicability, we use the limits $-1 \leq r \leq 1$, $0 \leq \vartheta \leq \pi/2$, and $0 \leq \varphi < 2\pi$ to uniquely identify the polar coordinates. Recapitulating Ref. 13, the entire spin dynamics in hybrid state is captured by the radius r of the magnetization, i.e., its magnitude combined with a sign, which is controlled only by the polar angle ϑ:

$$\dot{r}(t) = -\left(\frac{\cos^2\vartheta(t)}{T_1} + \frac{\sin^2\vartheta(t)}{T_2}\right)r(t) + \frac{\cos\vartheta(t)}{T_1} \tag{1}$$

Here, $\dot{r}(t)$ denotes the partial derivative of r with respect to time.

The flip angle and the phase of the radio frequency (RF) pulses, as well as the repetition time T_R have only an indirect and joint effect on the spin dynamics:

$$\tan\vartheta = \frac{\tan\frac{\alpha}{2}}{\sin\frac{\phi}{2}}, \tag{2}$$

where $\phi = \omega_z T_R$ describes the phase accumulated during one repetition time T_R and α denotes the flip angle. This equation reduces to $\vartheta = \alpha/2$ for $\phi = \pi$, which we define as the on-resonance condition. In practice, $\phi = \pi$ is assigned to the on-resonant spin isochromat by the common phase increment of π in consecutive RF pulses. Note that Equation (2) is equivalent to Equation (3) described by Schmitt et al[17] (given a different definition of ϕ), as well as to Equation (5) in Ref. 13. Further, Equation (1) generalizes the transient-state behavior described by Schmitt et al[6,17] to variable ϑ (cf. Equation (6) in Ref. 6 and the supporting information of Ref. 13).

In order to provide some intuition for the hybrid-state spin dynamics, we visualize its governing differential equation (Equation (1)) in Figure 1A. One can identify the so-called steady-state ellipse,[15–20] which separates areas of the Bloch sphere in which the magnetization grows (red) or shrinks (blue). The absolute value of the derivative of Equation (1) with respect to T_1 is in the upper limit twice as high on the southern hemisphere as it is on the northern hemisphere (note the asymmetric color bar in Figure 1B), which indicates that T_1 can be encoded faster on the southern hemisphere. A second benefit of inversion recovery experiments becomes evident when comparing the derivative with respect to T_1 (Figure 1B) to the one with respect to T_2 (Figure 1C). One changes sign between the hemispheres while the other does not. Thus, encoding data on the southern and northern

Author Manuscript Author Manuscript Author Manuscript Author Manuscript

hemisphere minimizes the correlation between the derivatives, which should yield a superior SNR in the estimated relaxation times by virtue of a lower Cramér-Rao bound[21,22] (cf. Equations (3)–(5)).

When considering T_1 only, Figure 1B suggests that there is a benefit in keeping the magnetization close to the z-axis on the southern hemisphere, and close to the origin on the northern hemisphere, since the absolute value of the derivative is largest in those areas. The derivative with respect to T_2, on the other hand, reaches its maximum far away from the z-axis (Figure 1C). This suggests that spin trajectories with large r may be desirable in order to probe these areas.

2.2 | Numerical optimizations

In order to verify this intuitive understanding, and to glean some insights on how to best probe the important areas of the Bloch sphere, we numerically optimize spin ensemble trajectories for a maximal SNR per unit time. To this end, the Cramér-Rao bound[21,22] is used to provide a universal limit for the noise variance of the estimated parameters. Given an unbiased estimator, i.e., the fitting algorithm used to calculate the proton density (M_0), T_1, and T_2, the noise variance of these parameters is at least as big as the corresponding Cramér-Rao lower bound. This very general and established metric has been utilized for optimizing MR parameter mapping experiments in Refs. [23–25] among others, and for MRF in particular in Ref. 26.

Assuming balanced gradient moments and small intravoxel dephasing, the hybrid state allows us to approximate a voxel's signal at the echo time $T_E = T_R/2$ by a single isochromat,[13] similar to balanced steady-state sequences.[27] With $s(t) = M_0 r(t) \sin \vartheta(t)$, where M_0 captures the complex valued proton density incl. coil sensitivity effects, we can calculate a discretized signal vector $\mathbf{s} \in \mathbb{C}^{1 \times N_t}$ from Equations (1) and (2). This vector describes the observed signal at N_t time points, and is used to calculate the Fisher information matrix $\mathbf{F} \in \mathbb{C}^{3 \times 3}$ whose entries are $\mathbf{F}_{i,j} = \mathbf{b}_i^H \mathbf{b}_j / \sigma^2$, where the vectors $\mathbf{b}_i$ describe the derivatives of the signal evolution with respect to all model parameters

$$\mathbf{b}_1 = d\mathbf{s}/\mathrm{d}M_0, \quad \mathbf{b}_2 = d\mathbf{s}/\mathrm{d}T_1, \quad \mathbf{b}_3 = d\mathbf{s}/\mathrm{d}T_2, \tag{3}$$

and the superscript H denotes the complex conjugate transposed. By normalizing with M_0, the input variance σ^2, the duration of the experiment $T_{\mathrm{exp}} = N_t T_R$, the repetition time T_R, and the squared relaxation time, we can define the relative Cramér-Rao bounds to be

$$rCRB(T_1) = M_0^2 \frac{\left(\mathbf{F}^{-1}\right)_{2,2}}{\sigma^2 T_1^2} \frac{T_{\mathrm{exp}}}{T_R} \tag{4}$$

$$rCRB(T_2) = M_0^2 \frac{\left(\mathbf{F}^{-1}\right)_{3,3}}{\sigma^2 T_2^2} \frac{T_{\mathrm{exp}}}{T_R}. \tag{5}$$

Author Manuscript Author Manuscript Author Manuscript Author Manuscript

The normalization by M_0^2 cancels out the M_0 scaling factor in the input signal, as does the σ^2 with the variance in the definition of the Fisher information matrix. The normalization by the squared relaxation time is performed in order to best reflect the $T_{1,2}$-to-noise ratio (defined as $T_{1,2}/\sigma_{T_{1,2}}$), and the normalization with T_{exp}/T_R makes the *rCRB* invariant to the number of measurements so that it describes the noise efficiency per unit time. In absolute numbers, the noise in the resulting parameter estimations is given by

$$\sigma_{T_{1,2}} \geq \frac{\sigma \cdot T_{1,2}}{M_0}\sqrt{rCRB(T_{1,2})\frac{T_R}{T_{\text{exp}}}}. \tag{6}$$

Note that the simulations published in Ref. 13 indicate that the actual noise in the estimated parameters is close to this bound. Without loss of generality, we assume $M_0 = 1$ for all theoretical considerations.

Given that ϑ is the effective drive of the spin dynamics,[13] we optimized ϑ directly and picked the sequence parameter (α, T_R, ϕ) retrospectively (cf. Equation (2)). Equation (1) is an uncoupled first order differential equation and can be solved for different boundary conditions.[13] Here, we focus on inversion-recovery balanced hybrid-state free precession (IR-bHSFP) sequences, i.e., hybrid-state sequences that depart from thermal equilibrium by the application of an inversion pulse, which is accounted for by the boundary condition $r(0) = -1$.

We used a Broyden-Fletcher-Goldfarb-Shanno (BFGS) algorithm[28] with $rCRB(T_1)$, $rCRB(T_2)$ and $rCRB(T_1) + rCRB(T_2)$ as objective functions. The numerical optimization was based on (nT_R) with the repetition time of $T_R = 4.5$ ms and with $n \in \{1, 2, \ldots, N_t\}$. The derivatives in Equation (3) were calculated analytically, as was the gradient of the objective function with respect to each (nT_R).

Since the *rCRB* intrinsically compares a fingerprint to its neighborhood in the parameter space, only a single set of relaxation times was used for the optimization. In particular, we used the relaxation times $T_1 = 781$ ms and $T_2 = 65$ ms, which correspond to values reported for white matter[1] at 3T. All optimizations were initialized with the pattern provided in Ref. 11.

We performed the above optimizations of IR-bHSFP sequence that exploit the full quadrant of the Bloch sphere ($0 \leq \vartheta \leq \pi/2$), and repeated the same optimizations with $0 \leq \vartheta \leq \pi/4$ in order to limit the flip angle to $\alpha \leq \pi/2$, ensuring consistent slice profiles by virtue of the linearity in the small tip-angle approximation,[29] and aiding compliance with safety considerations by avoiding high power large flip-angle pulses. For comparison, we also performed unconstrained optimizations of Look-Locker[30] and multi-spin-echo experiments.

2.3 | In vivo experiments

An asymptomatic volunteer's brain was imaged following written informed consent, and according to a protocol approved by our institutional review board. Measurements were performed with the IR-bHSFP sequences that minimize $rCRB(T_1)$, $rCRB(T_2)$ and $rCRB(T_1) + rCRB(T_2)$, limited to $0 \leq \vartheta \leq \pi/4$. All experiments were performed on a 3T Prisma

Author Manuscript Author Manuscript Author Manuscript Author Manuscript

scanner (Siemens, Erlangen, Germany). The 44 head elements of the manufacturer's 64 channel head/neck coil were used for signal reception. At the beginning of the sequence, a secant inversion pulse[31] with a duration of 10.24ms was applied, followed by a spoiler gradient. The other RF-pulses were implemented as slice-selective sinc pulses with a time-bandwidth product of two and a duration of 1 ms.

Spatial encoding was performed with a radial trajectory and a golden angle increment.[32] The spatial resolution of the maps is 1 mm × 1 mm × 3 mm at a FOV of 256 mm × 256 mm × 3 mm. The readout dwell time was set to 2.4 μs and an oversampling factor of 2 was applied. The total scan time of each sequence was approximately 3.8 s. In order to allow for a noise-analysis, we repeated the scan with each of the three sequences 49 times, separated by a 10 s pause in order to allow the magnetization to relax to thermal equilibrium. The k-space trajectory of consecutive scans were rotated by the tiny golden angle[33] $\varphi_{\mathrm{tGA}} \approx 32.04°$.

The raw data were compressed to eight virtual receive coils via SVD compression.[34] Thereafter, image reconstruction was performed with the low rank alternating direction method of multipliers[35,36] (ADMM) approach proposed in Ref. 37. A rank 6 subspace was estimated from a coarse dictionary[38] that was computed with Equations (1) and (2) and covered the range of T_1 values between 300 ms and 6 s and T_2 values in the range of 10 ms and 3 s, both in logarithmic steps of 10%. The data consistency step of the ADMM algorithm was performed with 20 conjugate gradient steps.

In the second step, the relaxation times were estimated with a nonlinear least-squared fit directly on the data in this low-rank sub-space. The fitting algorithm accounts for the slice profile and finite pulse duration[39] by approximating the profile by 12 isochromats, evenly distributed over the range with signal larger than 0.5% of the maximum value. For each of these isochromats, we calculated $\vartheta(t)$ with Bloch- simulations and retrospectively discretized this function to steps of 50 μs. This pre-calculated $\vartheta(t)$ was then plugged into the hybrid-state simulation based on Equation (1). Further, we correct for B_0 and B_1 based on separate scans with a double-echo SPGR and a turboFLASH[40] sequence, respectively. In order to prevent nonlinear effects from complicating the noise assessment, only a single ADMM iteration was performed and no spatial regularization was applied.

3 | RESULTS

3.1 | Spin dynamics on the Bloch sphere

Figure 2 depicts the hybrid-state spin ensemble trajectories and the corresponding driving functions $\vartheta(t)$ that were numerically optimized for T_1 and/or T_2 encoding. Some features are shared by all patterns, while others differ depending on the figure of merit. In the paragraphs that follow, the common features are described first, followed by the optimization-specific features.

All patterns are comparatively smooth, which is not explicitly enforced by the optimization. They start with a nonrecurring inversion segment on the southern hemisphere, followed by repetitive loops on the northern hemisphere. The beginning of the first loop differs slightly from that of the other loops, which can be explained by the initial conditions of the loop. At

Author Manuscript Author Manuscript Author Manuscript Author Manuscript

the time when the magnetization crosses the origin (turquoise segments in Figure 2), the derivatives with respect to the relaxation times are comparatively large. Furthermore, the derivative with respect to T_2 has not yet changed its sign. These two properties make this segment a valuable asset to help minimize the correlation between the derivatives with respect to the two relaxation times. As a consequence, the optimized trajectories have a comparatively large polar angle in this segment. In contrast, the subsequent loops start with a segment in which the magnetization recovers along the z-axis, reflecting small and correlated derivatives.

Another common feature of all trajectories is that the polar angle decreases rapidly when the shrinking magnetization reaches the steady-state ellipse (magnifications in Figure 2A, D, G, J, M, P). The arrival at the steady-state ellipse (blue ellipse in Figure 2) also concludes the last loop in the T_2-specific and in the jointly optimized patterns so that they take advantage of the T_2-dominated shrinkage of the magnetization (D, G, M, P). By contrast, the T_1-specific trajectories (A, J) conclude by maximizing r and $\mathrm{d}r/\mathrm{d}T_1$ and then briefly bringing the prepared magnetization close to the equator in order to maximize the signal.

Taking a closer look at the T_1-optimized hybrid-state pattern, we observe that the spin trajectory stays close to the z-axis on the southern hemisphere and close to the origin on the northern hemisphere (Figure 2A), which is exactly the behavior we expect from the intuitive understanding of the derivatives (Section 2.1). In fact, the numerical optimization suggests that it is beneficial to forgo any signal at the beginning of the sequence (dark blue segment) in favor of an information-rich signal thereafter. Comparing the unconstrained optimization ($0 \leq \vartheta \leq \pi/2$) with the constrained one ($0 \leq \vartheta \leq \pi/4$), we find that the spin trajectory remains virtually unaffected on the southern hemisphere (Figure 2J–L). On the northern hemisphere, however, the unconstrained pattern exploits the maximum polar angle of $\pi/2$ to quickly kill the magnetization and create a sort of saturation- recovery loop. When the polar angle is constrained, on the other hand, the magnetization shrinks more slowly and, consequently, fewer loops can be performed in the same amount of time.

When a hybrid-state sequence is optimized purely for T_2 encoding without constraining the polar angle, the magnetization first decays along the equator (Figure 2D), which is in agreement with the intuitive understanding described in Section 2.1. As r approaches zero, its derivatives with respect to the relaxation times become small as well and the spins follow a trajectory along the z-axis (bright blue segment). Thereafter, the spins follow large loops that probe the spin dynamics far from the z-axis where the derivative $\partial^2|I|/(\mathrm{d}t\mathrm{d}T_2)$ is large (cf. Figure 1C). Surprisingly, the optimization does not result in further segments with $\vartheta = \pi/2$. Instead, the trajectory traverses this value only briefly as the magnetization approaches the origin, before dropping to $\vartheta = 0$. Limiting the polar angle to $0 \leq \vartheta \leq \pi/4$ distorts the spin trajectory and the maximum value $\vartheta = \pi/4$ is exploited during several segments (M, N).

After the inversion pulse, the trajectory of the combined optimization oscillates between large and small ϑ-values. The corresponding derivatives of the magnetization have peaks that are shifted with respect to one another (Figure 2G–I). The size of the loops lies in between the ones of the T_1- and T_2-optimized trajectories. When the polar angle is limited to $0 \leq \vartheta \leq \pi/4$, the spin trajectory is distorted in a similar way as for the T_2-optimized case.

Author Manuscript Author Manuscript Author Manuscript Author Manuscript

The hybrid-state equation of spin motion (Equation (1)) can be written in a dimensionless form (Equation S1 in the supporting information), which highlights the fact that only the ratios T_{exp}/T_2 and T_1/T_2 of the involved time constants affect the hybrid-state spin trajectories. Varying T_{exp}/T_2 in the joint optimization results in different trade-offs between the inversion phase and the repetitive loops (see Supporting Information Figure S1). Short sequences ($T_{exp} \approx T_2$) require a T_2-optimized inversion phase similar to Figure 2M since the temporal constraints allow only for small, T_1-dominated loops. Increasing the sequence duration allows for larger loops so that the optimized inversion phase increasingly trades T_2 for T_1 encoding (cf. Figure 2P). Long sequences ($T_{exp} \gg T_2$) use a T_1-optimized inversion-recovery segment (cf. Figure 2J) followed by a combination of large loops, which predominantly encode T_2, and smaller loops, which provide additional T_1 encoding (Supporting Information Figure S1). In this limit, the shape of the loops changes little when varying T_{exp} and—considering the non-convexity of the optimization landscape—we can cautiously conclude that a combination of these two loops is superior to other loops, given the particular set of relaxation times.

Supporting Information Figure S2 analyzes the effect of T_1/T_2 variations on the spin ensemble trajectory and demonstrates that the optimized loop size decreases as the ratio between T_1 and T_2 increases. Large T_1 values limit how much the magnetization can grow within a given time. Therefore, the optimized ϑ-pattern spends most of the time for this recovery and the resulting loop size is small. One can further observe that the optimization of $rCRB(T_1) + rCRB(T_2)$ results in different trade-offs between T_1 and T_2 encoding at different T_1/T_2 ratios (Figure S2C). At intermediate ratios, the algorithm slightly favors the T_1-encoding, which is reflected both in the Cramér-Rao bound and in the corresponding spin ensemble trajectory, as evident by the inversion-recovery segment. Both at small and large ratios, the individual Cramér-Rao bounds are similar.

3.2 | The Cramér-Rao bound

This section analyzes the SNR-efficiency of different optimized spin ensemble trajectories. Examining $rCRB(T_1)$, we can observe that the purely T_1-optimized trajectories shine most at short experiment durations T_{exp} (Figure 3A).As the duration increases, the advantage of the T_1-optimized trajectories over the joint optimizations starts to vanish. At $T_{exp} = 3.8$ s, which is used for the in vivo experiments, we expect only a minor advantage of the T_1-optimized sequence in comparison to the joint optimization. In contrast, the T_2-optimized sequence shows a poor T_1-encoding power. Furthermore, we can see that the limit $\vartheta \leq \pi/4$ compared to $\vartheta \leq \pi/2$ has only minor effects on the T_1 and joint optimizations (light colored vs. dark colored marks in Figure 3). For comparison, we also show the Cramér-Rao bound of an optimized Look-Locker sequence[30] in which we also allowed the flip angle to vary over time. One can observe a substantially worse performance compared to the hybrid state, even if one is interested only in T_1.

Examining $rCRB(T_2)$, we also find the difference of the purely T_2-optimized and the jointly optimized sequences to be rather small (Figure 3B), especially when limiting the polar angle to $\pi/4$. The T_1-optimized patterns, on the other hand, show a poor T_2-encoding. For comparison, we also depict the Cramér-Rao bound of a multi-spin-echo sequence. For short

Author Manuscript Author Manuscript Author Manuscript Author Manuscript

experiments, this sequence has the same $rCRB(T_2)$ as the hybrid-state sequence that was optimized for T_2 without constraining ϑ. In fact, in this limit, both optimizations result in the same sequences (not shown here). For long experiments, however, the performance of the multi spin-echo sequence does degrade and the more general hybrid state allows for more efficient sequence design.

Overall, we can observe that the $rCRB$ has a minimum at $T_{\text{exp}} \approx T_1$. For longer T_{exp}, the Cramér-Rao bound asymptotically approaches a constant value, which corresponds to the standard averaging property $SNR \propto \sqrt{T_{\text{exp}}}$ of Gaussian noise. This is in line with the optimized spin trajectories in the limit of long T_{exp}, where a change in T_{exp} results in negligible changes in the shapes of the loops, instead merely adding averages over the same loop.

So far, the Cramér-Rao bound was analyzed only at the specific $T_1 = 781$ ms and $T_2 = 65$ ms that were used for the optimization. Figure 4 shows the performance of sequences optimized for these particular relaxation times over the range of T_1 and T_2 values commonly found in biological tissue. We found that optimizing for a single set of relaxation times does not merely result in good performance in the proximity of this set of parameters (visualized by the red dot), but over a large area in the T_1-T_2-space. In fact, the lowest Cramér-Rao bound is located at relaxation times different from those used during the optimization.

3.3 | Correlation coefficients

In order to relate the Cramér-Rao bound analysis in Figure 4 to the matching procedures commonly used in MRF, we calculated the correlation coefficient β between the dictionary atoms. Figure 5 depicts the correlation between the fingerprint corresponding $T_1 = 781$ ms and $T_2 = 65$ ms (red square) and the other fingerprints in the dictionary. These results are in good agreement with the $rCRB$ plots shown in Figure 4. Optimizing for a single relaxation time results in a comparably narrow peak of high correlation coefficients in the optimized dimension and a broad peak along the other dimension. The broadest peak is observed along T_2 in the T_1-optimized sequence, which is in agreement with the Cramér-Rao bound analysis (Figure 4). The joint optimization results in narrow peaks along both dimensions and confirms that adding a second relaxation time to the optimization has a very small penalty on the original relaxation time.

Figure 6 shows maximum intensity projections of the full correlation matrix among all fingerprints in the dictionary. These projections can be understood as the worst case correlations for a single parameter under consideration of all values of the other parameter. The generally larger $rCRB(T_2)$ compared to $rCRB(T_1)$ (cf. Figure 4) is reflected by the correlation coefficients. These findings confirm that the joint optimization results in encoding power that is comparable to respective specialized sequences. Further, the least precise encoding is along T_2 when using the T_1-optimized sequence, as already found in the Cramér-Rao bound analysis.

Author Manuscript Author Manuscript Author Manuscript Author Manuscript

3.4 | In vivo experiments

Figure 7 depicts quantitative in vivo maps acquired with the patterns shown in Figure 2K, N, Q. The total scan time of each experiment was 3.8 s. Systematic deviations can be noted in the measured relaxation times between the three sequences. This becomes even more evident when averaging the relaxation times over 49 experiments (Figure 8). Compared to literature (Table 1), we can observe a mild under-estimation of T_1, and T_2-values that are less than half of the relaxation times of ex vivo mouse samples, measured with an extensive protocol that does not have the time-, hardware-, and safety-related limitations we have for in vivo imaging. This underestimation is slightly less pronounced when using the T_2-optimized sequence.

Figure 9 verifies the noise properties predicted by the Cramér-Rao bound (Figure 4). As anticipated, the purely T_1-optimized pattern has superior noise performance in T_1, most notably in gray matter. This agrees with Figure 4A, which reveals a lower Cramér-Rao bound for longer relaxation times, as typically found for gray matter in comparison to white matter. The predicted poor T_2-encoding of the T_1-optimized sequence is also reflected in a low T_2/σ_{T_2}, especially in white matter (Figure 9D). We find a higher T_2/σ_{T_2} in gray matter, which is also in good agreement with the Cramér-Rao bound (Figure 4D). As predicted, the purely T_2-optimized and the jointly optimized sequences have very similar noise performance, with a slightly higher T_1/σ_{T_1} in the jointly optimized sequence (Figure 9B vs. C) and a slightly higher T_2/σ_{T_2} in the T_2-optimized sequence (Figure 9E vs. F).

4 | DISCUSSION

Steady-state free precession sequences[15] are known for their superior signal-to-noise efficiency. However, in first approximation, they only allow for a T_1/T_2 contrast, limiting their clinical versatility. In the context of quantitative MRI, it has been suggested to disentangle T_1 and T_2 information with a second measurement using an SPGR sequence,[4] or by exploiting deviations from this first order approximation.[42] The latter approach requires deviating from the on-resonance condition ($\phi = \pi$) and driving the magnetization into the stop band (i.e., the banding artifact). In the stop band, the spin-echo-like nature of the bSSFP sequence breaks down,[27] which introduces a sensitivity to the Larmor frequency distribution and can result in systematic errors in the presence of multiple spectral peaks.[43,44] Driving the magnetization's magnitude into a transient state, on the other hand, enables efficient encoding of T_1 and T_2 on resonance.[6,13] When the direction of the magnetization is maintained in a steady state, the spin-echo-like nature of the bSSFP sequence is preserved, and the signal response becomes comparatively robust to the frequency distribution.[13]

The hybrid state constitutes a large sequence design space, and the main purpose of this paper is to shed some light on the optimal encoding of spin relaxation times in this space. The adiabatic behavior of the magnetization's direction traps the spin dynamics in a single dimension. This reduces the equation of spin motion to a single, uncoupled first order differential equation (Equation (1)), which may be conveniently visualized (Figure 1). Insights gleaned from an intuitive understanding of the governing equation were found to align well with numerical optimizations (Figure 2). Numerically searching for the optimal

Author Manuscript Author Manuscript Author Manuscript Author Manuscript

spin trajectories is a non-convex problem, so we can only speculate about the optimality of our results. However, the notable correspondence to the intuitive understanding of the governing differential equation, together with the number of reproducible features in the optimized trajectories, gives us confidence that the obtained numerical results are closely related to the truly optimal trajectories.

The Cramér-Rao bound was used as figure of merit since it provides a universal lower bound for the noise transfer from a time series to the estimated parameters. It also provides the flexibility to tailor the acquisition to, e.g., encode T_1 while accounting for correlations in T_2-space. Within the limits of this analysis—most notably our neglect of the incomplete spatial encoding and the non-convexity of the optimization problems—we showed that the hybrid state has superior SNR properties compared to traditional methods, namely Look-Locker for T_1-encoding and multi-spin-echo sequences for T_2-encoding. Moreover, we found that the joint optimizations have nearly the same performance in encoding each relaxation time compared to hybrid-state sequences that are specialized to encode a single parameter. Thus, the second relaxation time can be measured at virtually no extra cost.

The *rCRB* has a minimum around $T_{\text{exp}} \approx T_1$. For a 2D multi-slice experiment, this suggests that one should use this optimal value and interleave multiple acquisitions of each slice. However, such short T_{exp} requires the repetition of power-consuming slice-selective inversion pulses that could exceed the overall SAR limit. Therefore, we used $T_{\text{exp}} \approx 3.8$ s as a compromise that allows for single-inversion imaging of a single slice with 1mm in-plane resolution.

Here, we optimized the sequences only for a single set of relaxation times, which correspond to values typical for white matter. However, we found that the resulting optimized sequences perform well over a large range of relaxation times. To extend this property further, one could optimize for the sum of the Cramér-Rao bounds at different relaxation times. Another option could be to minimize the maximum Cramér-Rao bound of multiple parameters and multiple parameter values. However, the non-linearity of such norms might impair the convergence of the optimization.

Our least-constrained optimizations used the limits $-1 \leq r(t) \leq 1$ and $0 \leq \vartheta(t) \leq \pi/2$. This unusual definition of spherical coordinates was chosen to deliberately prohibit magnetization from revisiting the southern hemisphere after passing through the origin. This allows us to implement the RF-pulses without major violations of the small tip-angle approximation. However, we demonstrated the benefits of the southern hemisphere and for long experiments as might be required, e.g., for 3D imaging, it might be desirable to revisit the southern hemisphere. This could be achieved by simply changing the limits to $0 \leq r(t) \leq 1$ and $0 \leq \vartheta(t) \leq \pi$. However, this would change the optimization landscape, and the convergence behavior might be impaired. Alternatively, one could use anti-periodic boundary conditions, as demonstrated in Ref. 13.

The primary purpose of the present work was to analyze the noise properties of hybrid-state sequences when quantifying relaxation times. Even though we correct for B_0 and B_1^+ inhomogeneities, as well as the slice profile and the finite duration of the RF-pulses, we

Author Manuscript Author Manuscript Author Manuscript Author Manuscript

found substantial systematic errors in the relaxation times measured in vivo (Figures 7 and 8), whereas, in previous work, we demonstrated good agreement between hybrid-state and gold standard measurements in a phantom.[13] It is known that the Bloch equation applies well to uniform liquids, but is an over-simplification of signal acquired in biological tissue as it neglects diffusion-mediated dephasing and magnetization transfer effects, among others.[41,45–49] Since the hybrid-state model was derived from the standard Bloch equation, it inherits this oversimplification, and we believe this to be the predominant cause for the systematic deviations from literature values.

Simultaneously avoiding diffusion-mediated dephasing and magnetization transfer is a key challenge for in vivo relaxometry. The decay of the transverse magnetization occurs on two distinct scales.[48] At the molecular level, the intrinsic T_2-relaxation originates from molecular rotations with a correlation time on the order of nanoseconds.[50,51] The cellular scale, present in biological tissues, provides a different relaxation mechanism, where spins diffuse through susceptibility-induced magnetic fields varying on the scale of ~1-10 μm, causing temporal field fluctuations with a correlation time of ~1-100 ms, depending on the tissue composition.[45–48] This loss of coherence can be partially undone by applying refocusing pulses. Since the timing of standard MR pulse sequences is exactly in this range, the overall T_2-relaxation crucially depends on the specifics of the sequence. Thus, measuring the intrinsic, molecular T_2 in vivo requires employing refocusing pulses with echo-spacing shorter than the corresponding correlation time. Depending on the tissue, standard CPMG[52] and bSSFP sequences,[15,27] as well as balanced hybrid-state sequences[13] approximate this requirement well. Therefore, we believe diffusion-mediated dephasing to be negligible in the hybrid-state. However, the repeated refocusing in any of those sequences requires a high duty cycle of the RF-pulses. In biological tissue, this saturates the magnetization of protons bound in macro-molecules, which are found in myelin, cell membranes, etc.[53,54] Therefore, apart from some very time-consuming methods,[41,49] most standard methods for measuring relaxation times are corrupted by cross-relaxation between the macro-molecular and the free water pool. We attribute the systematic errors observed here (Figure 8) to this effect, similar to Ref. 55. Note that the hybrid state model can be extended to include magnetization transfer,[56] and our preliminary data indicate that such a model describes the spin dynamics in good agreement with literature.

5 | CONCLUSION

The goal of this paper was to provide insights into optimized encoding of spin relaxation times in order to guide the design of robust and efficient pulse sequences. We reviewed how the Bloch equation can be simplified under the hybrid-state adiabaticity condition and demonstrated the intuition that can be gained from this simplification. Further, we showed that numerical optimizations of hybrid-state sequences reproducibly converge to spin trajectories that align well with intuitive understanding. We analyzed the SNR efficiency of the optimized hybrid-state sequences, demonstrated superior efficiency in comparison to traditional methods, and highlighted the good agreement between theoretical Cramér-Rao bounds and experimentally-observed noise properties. Future work will translate the insights gained in this work to hybrid-state models that include more complex phenomena, such as

Author Manuscript Author Manuscript Author Manuscript Author Manuscript

magnetization transfer, which we consider central for fast and reproducible quantification of tissue properties.

Supplementary Material

Refer to Web version on PubMed Central for supplementary material.

Acknowledgments

Funding information

NIH/NIBIB, Grant/Award Number: R21 EB020096; NIH/NIAMS, Grant/Award Number: R01 AR070297; NIH/NIBIB, Grant/Award Number: P41 EB017183.

REFERENCES

1. Jiang Y, Ma D, Seiberlich N, Gulani V, Griswold MA. MR fingerprinting using fast imaging with steady state precession (FISP) with spiral readout. Magn Reson Med. 2015;74:1621–1631. [PubMed: 25491018]
2. Crawley AP, Henkelman RM. A comparison of one-shot and recovery methods in T_1 imaging. Magn Reson Med. 1988; 7: 23–34. [PubMed: 3386519]
3. Cheng HLM, Wright GA. Rapid high-resolution T_1 mapping by variable flip angles: accurate and precise measurements in the presence of radiofrequency field inhomogeneity. Magn Reson Med. 2006;55:566–574. [PubMed: 16450365]
4. Deoni SCL, Rutt BK, Peters TM. Rapid combined T_1 and T_2 mapping using gradient recalled acquisition in the steady state. Magn Reson Med. 2003;49:515–526. [PubMed: 12594755]
5. Deoni SCL, Peters TM, Rutt BK. Determination of optimal angles for variable nutation proton magnetic spin-lattice, T_1, and Spin-Spin, T_2, relaxation times measurement. Magn Reson Med. 2004;51:194–199. [PubMed: 14705061]
6. Schmitt P, Griswold MA, Jakob PM, et al. Inversion recovery TrueFISP: quantification of T_1, T_2, and spin density. Magn Reson Med. 2004;51:661–667. [PubMed: 15065237]
7. Ehses P, Seiberlich N, Ma D, et al. IR TrueFISP with a golden-ratio-based radial readout: fast quantification of T1, T2, and proton density. Magn Reson Med. 2013;69:71–81. [PubMed: 22378141]
8. Ma D, Gulani V, Seiberlich N, et al. Magnetic resonance fingerprinting. Nature 2013;495:187–192. [PubMed: 23486058]
9. Cloos MA, Knoll F, Zhao T, et al. Multiparamatric imaging with heterogenous radiofrequency fields. Nat Commun. 2016;7. doi:10.1038/ncomms12445.
10. Ma D, Pierre EY, Jiang Y, et al. Music-based magnetic resonance fingerprinting to improve patient comfort during MRI examinations. Magn Reson Med. 2016;75:2303–2314. [PubMed: 26178439]
11. Assländer J, Glaser SJ, Hennig J. Pseudo steady-state free precession for MR-fingerprinting. Magn Reson Med. 2017;77:1151–1161. [PubMed: 27079826]
12. Jiang Y, Ma D, Jerecic R, et al. MR fingerprinting using the quick echo splitting NMR imaging technique. Magn Reson Med. 2017;77:979–988. [PubMed: 26924639]
13. Assländer J, Novikov DS, Lattanzi R, Sodickson DK, Cloos MA. Hybrid-state free precession in nuclear magnetic resonance. Nat Commun Phys. 2019. doi:10.1038/s42005-019-0174-0.
14. Ganter C Off-resonance effects in the transient response of SSFP sequences. Magn Reson Med. 2004;52:368–375. [PubMed: 15282820]
15. Carr H Steady-state free precession in nuclear magnetic resonance. Phys. Rev. 1958;112:1693–1701.
16. Tahayori B, Johnston LA, Mareels IMY, Farrell PM. Novel insight into magnetic resonance through a spherical coordinate framework for the Bloch equation. SPIE Conf Med Imaging 2009;7258:2–4.

Author Manuscript Author Manuscript Author Manuscript Author Manuscript

17. Schmitt P, Griswold MA, Gulani V, Haase A, Flentje M, Jakob PM. A simple geometrical description of the TrueFISP ideal transient and steady-state signal. Magn Reson Med. 2006;55:177–186. [PubMed: 16323155]
18. Freeman R, Hill HDW. Phase and intensity anomalies in fourier transform NMR. J Magn Reson. 1971;4:366–383.
19. Hennig J, Speck O, Scheffler K. Optimization of signal behavior in the transition to driven equilibrium in steady-state free precession sequences. Magn Reson Med. 2002;48:801–809. [PubMed: 12417994]
20. Lapert M, Assémat E, Glaser SJ, Sugny D. Understanding the global structure of two-level quantum systems with relaxation: vector fields organized through the magic plane and the steady-state ellipsoid. Phys Rev A. 2013;88:033407.
21. Rao CR. Information and the accuracy attainable in the estimation of statistical parameters. Bull Calcutta Math Soc. 1945;37:81–91.
22. Cramér H Methods of Mathematical Statistics. Princeton, NJ: Princeton University Press, 1946.
23. Jones J, Hodgkinson P, Barker A, Hore P. Optimal sampling strategies for the measurement of spin–spin relaxation times. J Magn Reson Ser B. 1996;113:25–34.
24. Jones JA. Optimal sampling strategies for the measurement of relaxation times in proteins. J Magn Reson. 1997;126:283–286.
25. Teixeira RPAG, Malik SJ, Hajnal JV. Joint System Relaxometry (JSR) and Crámer-Rao lower bound optimisation of sequence parameters: a framework for enhanced precision of DESPOT T_1 and T_2 estimation. Magn Reson Med. 2018;79:234–245. [PubMed: 28303617]
26. Zhao B, Haldar JP, Setsompop K, Wald LL. Optimal experiment design for magnetic resonance fingerprinting. In: i and Biology Society; 2016:453–456.
27. Scheffler K, Hennig J. Is TrueFISP a gradient-echo or a spin-echo sequence? Magn Reson Med. 2003;49:395–397. [PubMed: 12541263]
28. De Fouquieres P, Schirmer SG, Glaser SJ, Kuprov I. Second order gradient ascent pulse engineering. J Magn Reson. 2011;212:412–417. [PubMed: 21885306]
29. Hoult DI. The solution of the bloch equations in the presence of a varying B_1 field-an approach to selective pulse analysis. J Magn Reson. 1979;35:69–86.
30. Look DC, Locker DR. Time saving in measurement of NMR and EPR relaxation times. Rev Sci Instrum. 1970;41:250–251.
31. Silver MS, Joseph RI, Hoult DI. Selective spin inversion in nuclear magnetic resonance and coherence optics through an exact solution of the Bloch-Riccati equations. Phys Rev A 1985;31:2753–2755.
32. Winkelmann S, Schaeffter T, Koehler T, Eggers H, Doessel O. An optimal radial profile order based on the golden ratio for time-resolved MRI. IEEE Trans Med Imaging 2007;26:68–76. [PubMed: 17243585]
33. Wundrak S, Paul J, Ulrici J, Hell E, Rasche V. A small surrogate for the golden angle in time-resolved radial MRI based on generalized fibonacci sequences. IEEE Trans Med Imaging 2015;34:1262–1269. [PubMed: 25532172]
34. Buehrer M, Pruessmann KP, Boesiger P, Kozerke S. Array compression for MRI with large coil arrays. Magn Reson Med. 2007;57:1131–1139. [PubMed: 17534913]
35. Boyd S, Parikh N, E Chu BP, Eckstein J. Distributed optimization and statistical learning via the alternating direction method of multipliers. Found Trends Mach Learn. 2011;3:1–122.
36. Zhao B, Setsompop K, Ye H, Cauley SF, Wald LL. Maximum likelihood reconstruction for magnetic resonance fingerprinting. IEEE Trans Med Imaging 2016;35:1812–1823. [PubMed: 26915119]
37. Assländer J, Cloos MA, Knoll F, Sodickson DK, Hennig J, Lattanzi R. Low rank alternating direction method of multipliers reconstruction for MR fingerprinting. Magn Reson Med. 2018;79:83–96. [PubMed: 28261851]
38. McGivney D, Ma D, Saybasili H, Jiang Y, Griswold M. Singular value decomposition for magnetic resonance fingerprinting in the time domain. IEEE Trans Med Imaging 2014;33:2311–2322. [PubMed: 25029380]

Author Manuscript Author Manuscript Author Manuscript Author Manuscript

39. Ma D, Coppo S, Chen Y, et al. Slice profile and B_1 corrections in 2D magnetic resonance fingerprinting. Magn Reson Med. 2017;78:1781–1789. [PubMed: 28074530]
40. Chung S, Kim D, Breton E, Axel L. Rapid B_1^+ mapping using a preconditioning RF pulse with turboFLASH readout. Magn Reson Med. 2010;64:439–446. [PubMed: 20665788]
41. Stanisz GJ, Odrobina EE, Pun J, et al. T_1, T_2 relaxation and magnetization transfer in tissue at 3T. Magn Reson Med. 2005;54:507–512. [PubMed: 16086319]
42. Shcherbakova Y, Berg VDCA, Moonen CT, Bartels LW. PLANET: an ellipse fitting approach for simultaneous T_1 and T_2 mapping using phase-cycled balanced steady-state free precession. Magn Reson Med. 2018;79:711–722. [PubMed: 28543430]
43. Shcherbakova Y, Berg VDCA, Moonen CT, Bartels LW. On the accuracy and precision of PLANET for multiparametric MRI using phasecycled bSSFP imaging. Magn Reson Med. 2019;81:1534–1552. [PubMed: 30303562]
44. Miller KL. Asymmetries of the balanced SSFP profile. Part I: theory and observation. Magn Reson Med. 2010;63:385–395. [PubMed: 20099328]
45. Jensen JH, Chandra R. NMR relaxation in tissues with weak magnetic inhomogeneities. Magn Reson Med. 2000;44:144–156. [PubMed: 10893533]
46. Kiselev VG, Novikov DS. Transverse NMR relaxation as a probe of mesoscopic structure. Phys Rev Lett. 2002;89:278101. [PubMed: 12513247]
47. Novikov DS, Kiselev VG. Transverse NMR relaxation in magnetically heterogeneous media. J Magn Reson. 2008;195:33–39. [PubMed: 18824379]
48. Kiselev VG, Novikov DS. Transverse NMR relaxation in biological tissues. Neuroimage 2018;182:149–168. [PubMed: 29885485]
49. Stanisz GJ, Kecojevic A, Bronskill MJ, Henkelman RM. Characterizing white matter with magnetization transfer and T_2. Magn Reson Med. 1999;42:1128–1136. [PubMed: 10571935]
50. Bloch F Nuclear induction. Phys Rev. 1946;70:460–474.
51. Bloembergen N, Purcell EM, Pound RV. Relaxation effects in nuclear magnetic resonance absorption. Phys Rev. 1948;73:679–712.
52. Meiboom S, Gill D, Gillt D. Modified spin-echo method for measuring nuclear relaxation times. Rev Sci Instrum. 1958;29:688–691.
53. Edzes HT, Samulski E. Cross Relaxation and spin diffusion in the proton NMR of hydrated collagen. Nature 1977;265:521–523. [PubMed: 834303]
54. Wolff SD, Balaban RS. Magnetization transfer contrast (MTC) and tissue water proton relaxation in vivo. Magn Reson Med. 1989;10:135–144. [PubMed: 2547135]
55. Hilbert T, Knoll F, Zhao T, et al. Magnetic resonance fingerprinting: mitigating the Bias in the quantification of T1 and T2 caused by macromolecules. Radiological Society of North America 2016 Scientific Assembly and Annual Meeting; 2016 http://archive.rsna.org/2016/16010335.html.
56. Assländer J, Sodickson DK. Quantitative magnetization transfer imaging in the hybrid state. In Proceedings of the 28th Annual Meeting of ISMRM, Montreal, Canada, 2019 Abstract 1104.

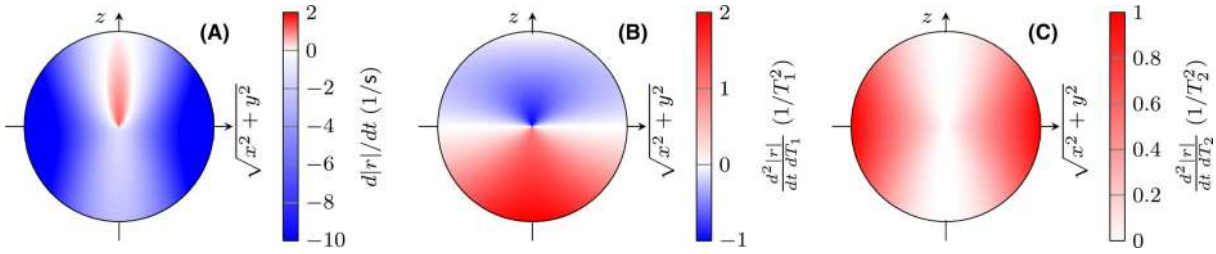

FIGURE 1.

Equation (1) describes the spin dynamics and is visualized in (A). The white area indicates the steady-state ellipse which separates the area in which the magnetization grows (red) and shrinks (blue). This particular sub-figure is valid for the ratio T_1/T_2 = 781 ms/65 ms ≈ 12, which are values reported for brain white matter.[1] The derivatives of Equation (1) with respect to T_1 and T_2 are depicted in (B) and (C), respectively. These plots are normalized by the respective relaxation times and are, therefore, valid for any combination of T_1 and T_2

Author Manuscript Author Manuscript Author Manuscript Author Manuscript

Author Manuscript Author Manuscript Author Manuscript Author Manuscript

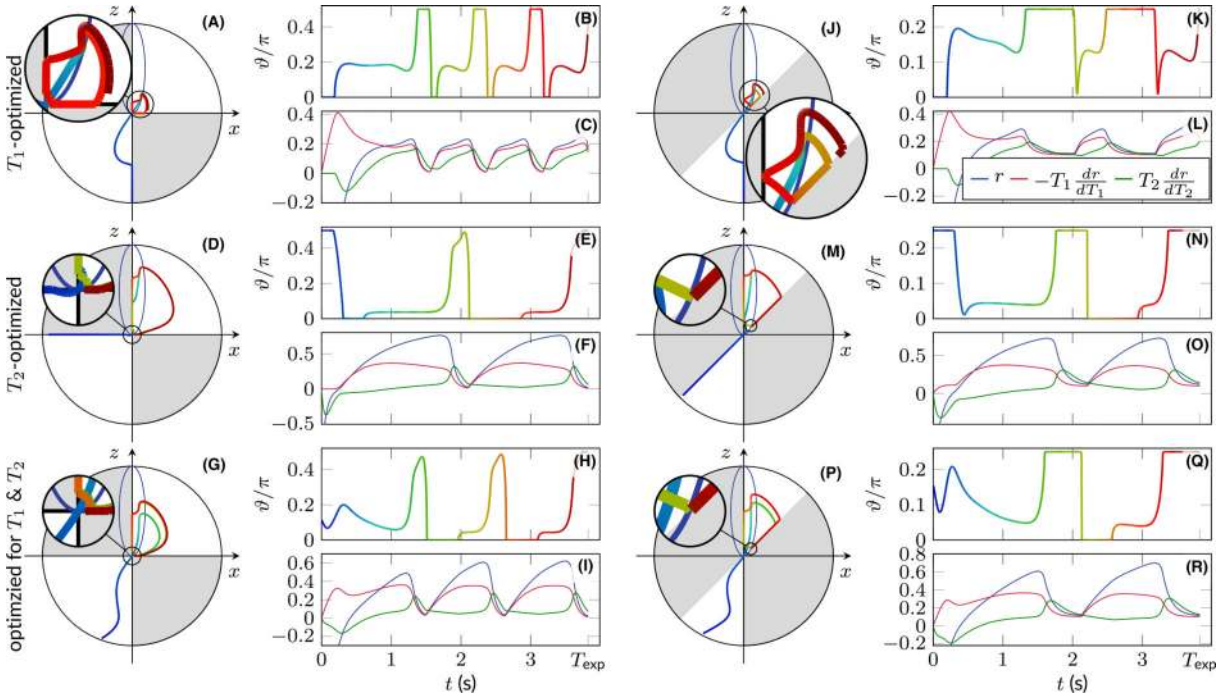

FIGURE 2.

The spin dynamics in inversion recovery balanced hybrid-state free precession (IR-bHSFP) sequences are depicted on Bloch-spheres (A, D, G, J, M, and P). The polar angle patterns are shown in (B, E, H, K, N, and Q), with the color scale providing a reference for the trajectories on the Bloch-sphere. The absolute value of the magnetization (with a negative sign indicating the southern hemisphere) and its normalized derivatives with respect to the relaxation times are the foundation of the relative Cramér-Rao bound and are shown in (C, F, I, L, O, and R). The optimizations depicted in the left-hand column are limited to $0 \leq \vartheta \leq \pi/2$, while the right-hand column shows the same optimizations with the limit $0 \leq \vartheta \leq \pi/4$

Author Manuscript Author Manuscript Author Manuscript Author Manuscript

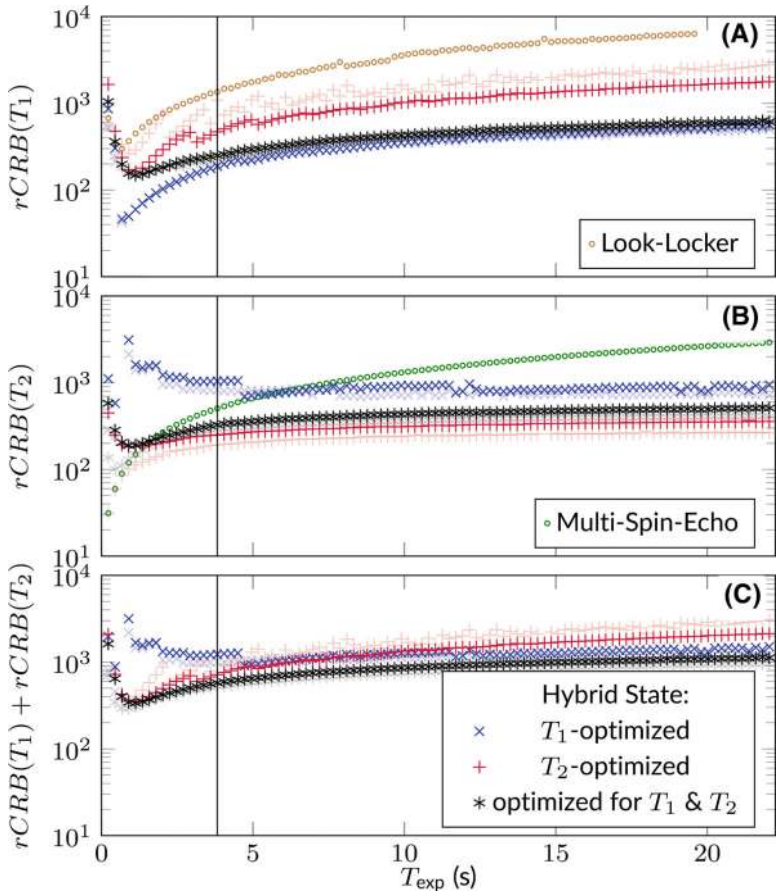

FIGURE 3.

The depicted relative Cramér-Rao bounds are defined by Equations (4) and (5) and can be understood as a lower bound of the squared inverse SNR efficiency per unit time. They result from numerical optimization for *rCRB*(T_1), *rCRB*(T_2), and *rCRB*(T_1) + *rCRB*(T_2), while limiting the polar angle to $0 \leq \vartheta \leq \pi/2$ (lightly colored markers) and $0 \leq \vartheta \leq \pi/4$ (dark colored markers), respectively

Author Manuscript Author Manuscript Author Manuscript Author Manuscript

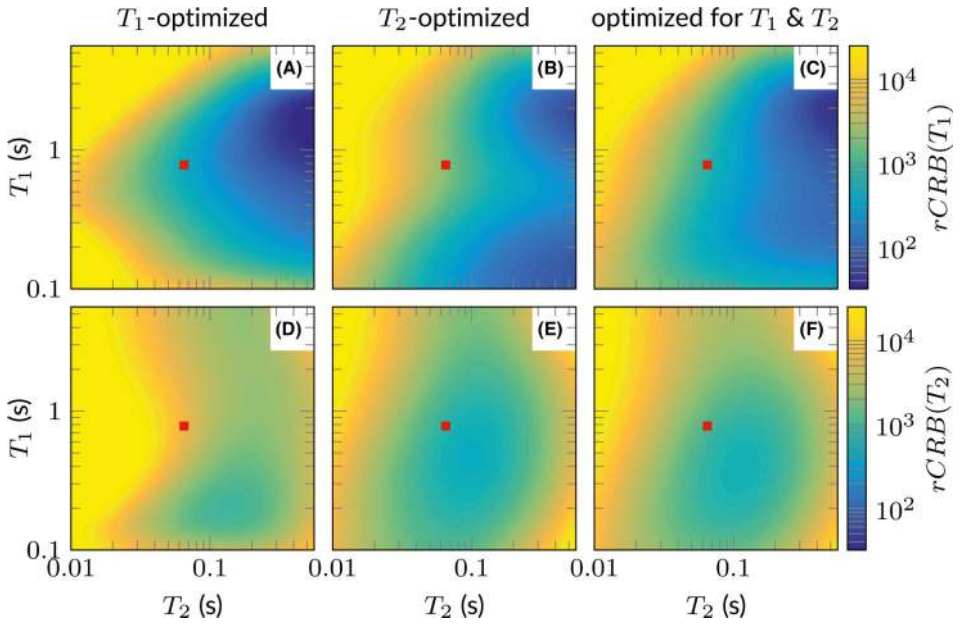

FIGURE 4.

The performance of IR-bHSFP sequences optimized with $0 \leq \vartheta \leq \pi/4$ (Figure 2J–R) is illustrated through plots of the relative Cramér-Rao bounds, which provide a lower bound for the noise in the estimated relaxation times. All patterns were optimized for T_1 = 781 ms and T_2 = 65 ms, as indicated by the red square, and were tested for the entire parameter space in a sample MRF dictionary. Note the logarithmic scale in all three dimensions

Author Manuscript Author Manuscript Author Manuscript Author Manuscript

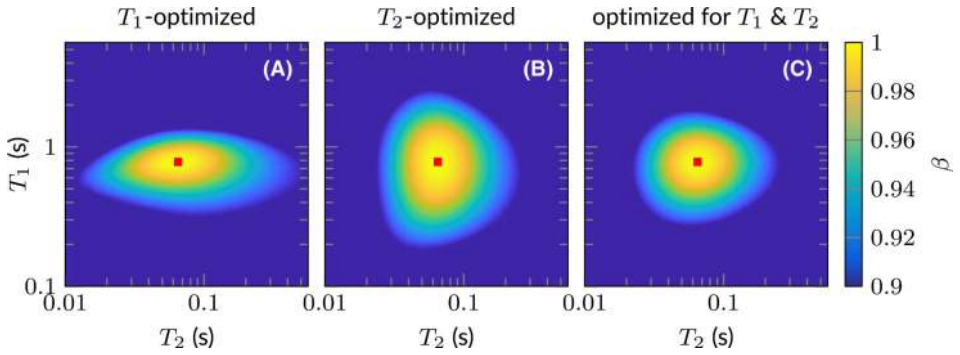

FIGURE 5.

The performance of IR-bHSFP optimized with $0 \leq \vartheta \leq \pi/4$ (Figure 2J–R) is illustrated through plots of the correlation of the fingerprint using the optimization parameters T_1 = 781 ms and T_2 = 65 ms (red square) with the rest of the parameter space

Author Manuscript Author Manuscript Author Manuscript Author Manuscript

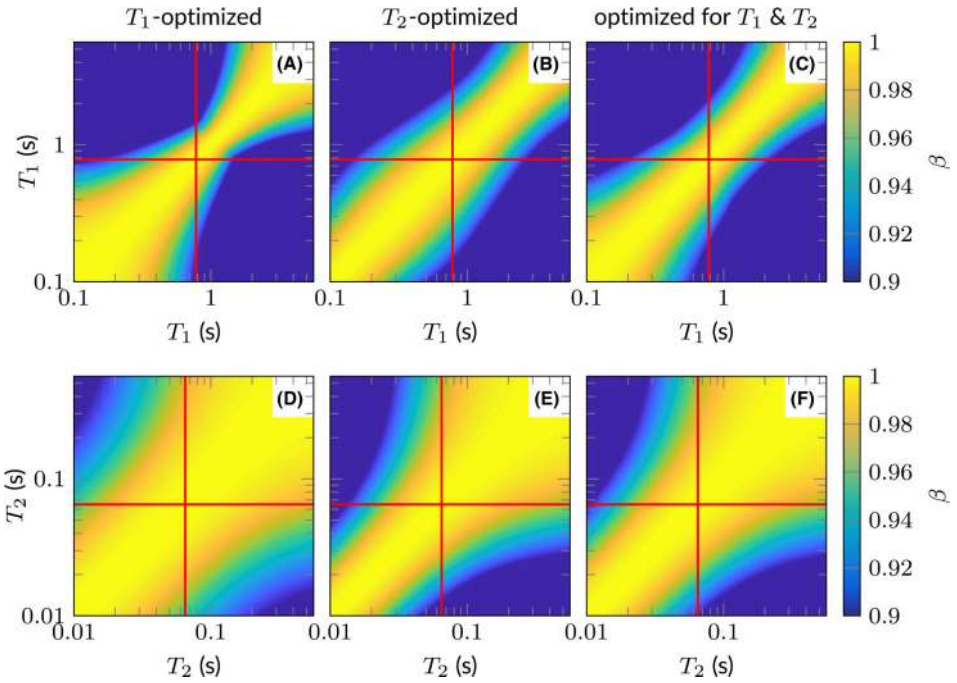

FIGURE 6.

The performance of IR-bHSFP optimized with $0 \leq \vartheta \leq \pi/4$ (Figure 2J–R) is depicted through plots of the correlation coefficient. The correlation matrix was calculated for the entire parameter space. Thereafter, a maximum intensity projection was performed along the T_2 (A-D) and the T_1-dimension (E-H), respectively. The result can be understood as the worst case correlations for a single parameter under consideration of all values of the other parameter. The red lines indicates the set of parameters used for optimizing the patterns

Author Manuscript Author Manuscript Author Manuscript Author Manuscript

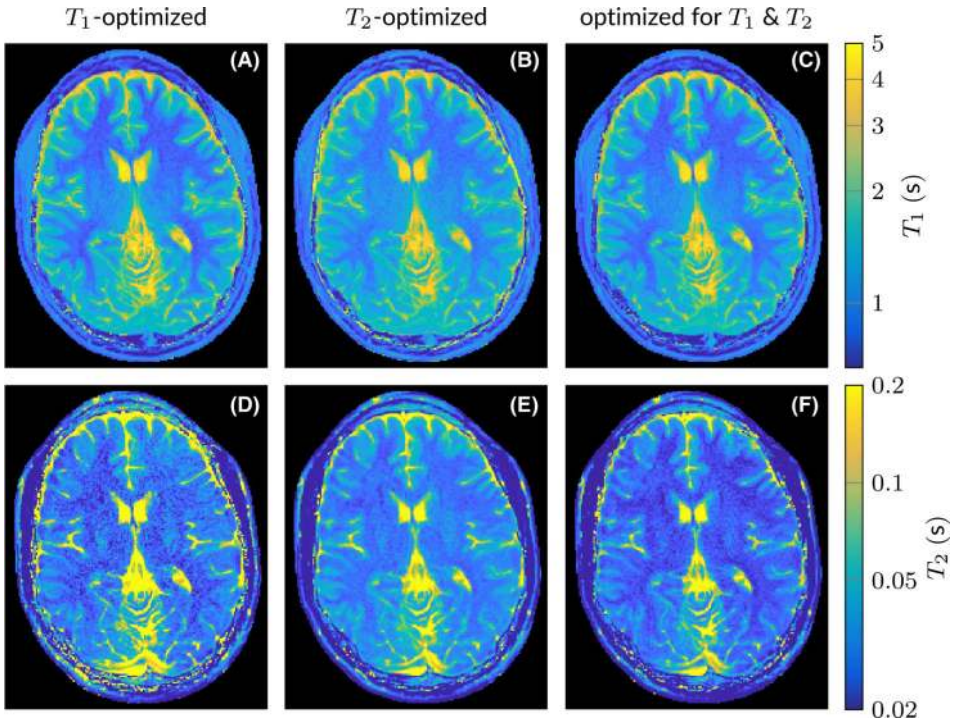

FIGURE 7.

The in vivo data were acquired with the excitation patterns depicted in Figure 2K, N, and Q with the limit $0 \leq \vartheta \leq \pi/4$. The parameter maps have an in-plane resolution of 1 mm and were acquired in 3.8 s. Note the logarithmic scale of the T_1 and T_2 color maps

Author Manuscript Author Manuscript Author Manuscript Author Manuscript

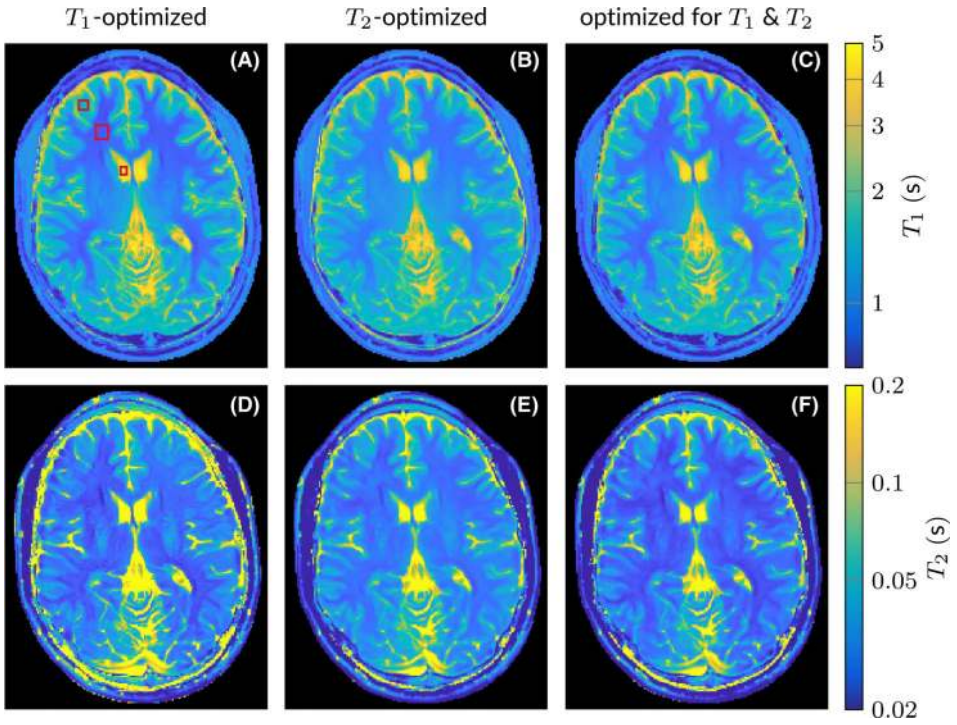

FIGURE 8.

The parameter maps are the average of 49 measurements like the one shown in Figure 7, each acquired in 3.8 s with a 10 s pause in between. Note the logarithmic scale of the T_1 and T_2 color maps. The red rectangles indicate the regions of interest used for calculating the values in Table 1

Author Manuscript Author Manuscript Author Manuscript Author Manuscript

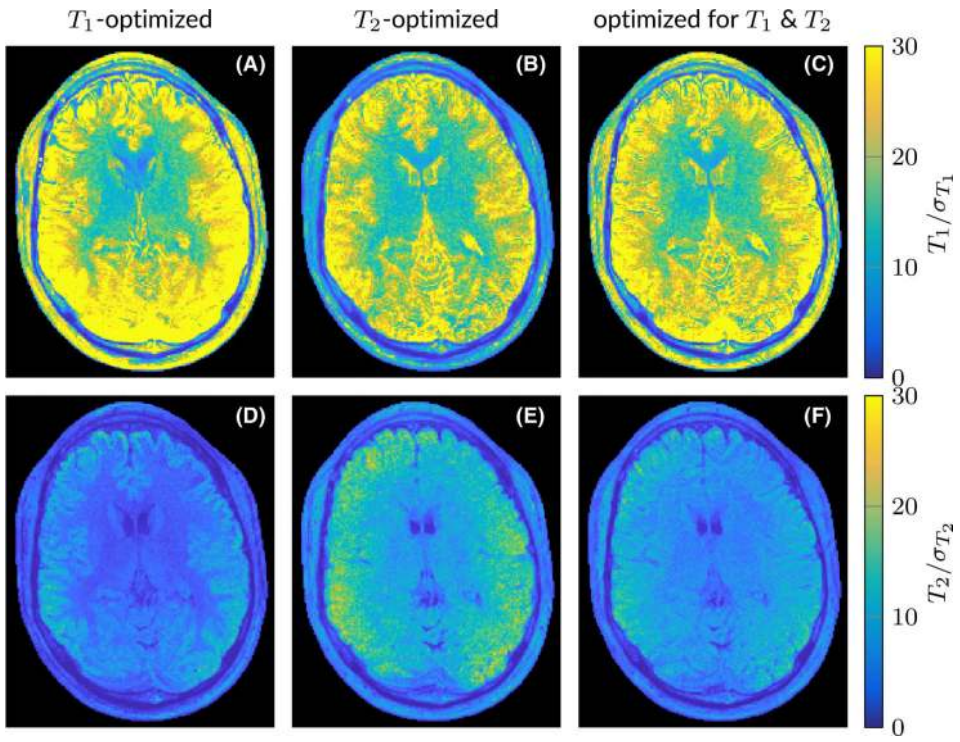

FIGURE 9.

In order to verify the theoretically derived noise properties, we depict the mean relaxation times divided by the standard deviation over the 49 consecutive experiments. This metric provides an analog to the signal-to-noise ratio. The upper limit of this metric is directly proportional to the square root of the inverse $rCRB(T_{1,2})$

Author Manuscript Author Manuscript Author Manuscript Author Manuscript

TABLE 1

The relaxation times are the mean values depicted in Figure 8 and the standard deviation (cf. Figure 9) of the 49 experiments, both averaged over respective region of interest. Therefore, the standard deviation does not reflect biological variations over the region of interest and is dominated by thermal noise

	White matter		Gray matter		CSF	
	T_1 (ms)	**T_2 (ms)**	**T_1 (ms)**	**T_2 (ms)**	**T_1 (ms)**	**T_2 (ms)**
T_1-optimized	961 ± 59	29.9 ± 5.5	1789 ± 48	43.7 ± 4.0	4494 ± 378	1421 ± 782
T_2-optimized	1100 ± 75	33.7 ± 2.8	1738 ± 60	48.6 ± 2.5	4256 ± 223	1642 ± 969
optimized for T_1 & T_2	963 ± 59	29.4 ± 3.2	1672 ± 55	43.0 ± 3.1	4354± 215	1079 ± 647
Ref. 41	1084 ± 45	69 ± 3	1820 ± 114	99 ± 7		